THERMAL DIFFUSION OF ALKALI METALS IN MERCURY'S REGOLITH

Cassandre Morel[1], Adam Woodson (advisor)[1]
[1]University of Virginia, Department of Materials Science and Engineering, Charlottesville, VA 22904, USA
April 7, 2025

Abstract Mercury is an airless body that undergoes several processes to replenish its exosphere. One of these low energy processes is thermal desorption, where parts of the surface with higher temperatures experience an increase in ejected volatiles like sodium. However, the exospheric sodium concentration patterns do not follow the predictions of our current models, which indicates that desorption processes are not as well understood as previously thought. In order to study the desorption rates, we simulated Mercury's surface conditions through a molecular dynamics code LAMMPS and tracked the motion of deposited sodium. After choosing the Pedone 2006 potential for the forsterite (Mg_2SiO_4) bulk and the Lennard Jones potential for the Na interactions, we conducted a cutoff distance survey in order to match realistic behaviors from previous laboratory experiments. This value was determined to be 2.6 Å, and we shifted our focus to Na residence times. Temperature was found to greatly affect Na residence times, where higher temperatures resulted in increased total desorption and a growing average residence time. Similar simulations will be run again in the future for better statistics.

Introduction

About 0.4 AU away from the Sun resides Mercury, a rocky, airless body that is enveloped by a tenuous exosphere. This thin layer of gas has a particle density so low (~10^5 particles per cubic centimeter) that the particles experience little to no interactions with each other (Domingue et al. 2007). If an airless body undergoes no replenishing processes, its exosphere will eventually be lost due to factors like Jean's escape, solar radiation pressure, and pick-up ion loss. On Mercury, however, there are several processes with varying levels of energy that contribute to exospheric creation and maintenance, as seen in Figure 1.

High energy processes, like micrometeoroid impact vaporization and solar wind ion sputtering, remove surface atoms with enough energy that they orbit the body and populate the exosphere, while some are pushed into a "tail" by solar radiation pressure as the body orbits around the Sun (Szabo et al. 2018; Wurz et al. 2022). Ion sputtering consists of highly energetic (~1 keV/amu) ions originating from the Sun that strike atoms present within minerals of Mercury's surface, which are subsequently sputtered away (Hundhausen et al., 1970; King & Papitashvili et al., 2005). For lower energy processes, the ejected atoms are redeposited over the surface as a fresh adsorbate layer, ready to be removed once again. Such processes include photodesorption, where photons break the bonds of adsorbed atoms, as well as thermal desorption, where atoms in warmer regions on the surface get excited and leave the surface.

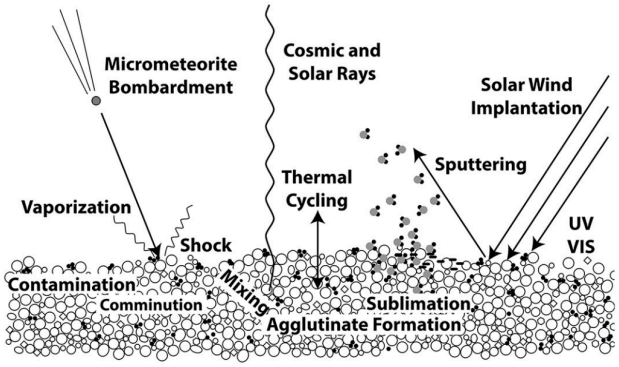

Figure 1 Processes that are responsible for creating and replenishing an exosphere on airless bodies (Szalay et al. 2018).

There are Na reservoirs present within the surface layers. Mercury's exosphere is likely constantly replenished with volatiles such as Na as they are released from the

planet's surface. Current predictions state that Na density in the exosphere would reach a peak at local noon, and the plume should be fully depleted soon after (Cassidy et al. 2016). The surface at local noon would be exposed to the maximum amount of sunlight and heat, triggering the photodesorption and thermal desorption processes more intensely than at any other time of the day. However, this does not seem to be the case as seen in Figure 2.

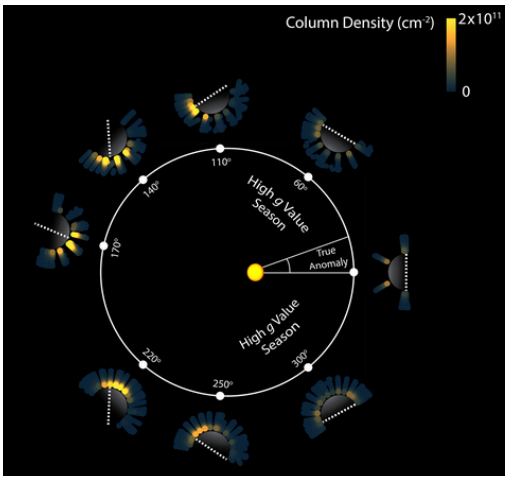

Figure 2 Density of sodium in the exosphere as Mercury rotates and revolves around the Sun (Cassidy et al. 2016).

As shown in Figure 2, the MESSENGER UltraViolet and Visible spectrometer measured density enhancements in Mercury's dayside exosphere that persist beyond local noon, contrary to current models. This indicates that the desorption processes on Mercury are still not properly understood. Diffusion of the alkali metals along and within the surface, as well as the presence of a massive sodium reservoir in the poles could explain this lagging peak concentration effect (Verkercke et al. 2024). Additionally, we have experimentally observed reduced Na sputter depletion rates for granular regolith-like targets (paper in preparation), which may also delay depletion of surface Na. To investigate these concerns, we ran simulations of a system modeled after Mercury's mineralogical surface and monitored the motion of deposited sodium atoms.

Mercury's surface is compositionally heterogeneous, where the outer crust of the planet consists of patches of various minerals. Due to the complex composition of this surface, modeling it requires some simplifications. A significant number of these patches likely consist of forsterite (Mg_2SiO_4), which is the magnesium-rich end member of the olivine solid solution. Since forsterite is devoid of sodium, we used forsterite as our bulk material so that we would not have to worry about separating the bulk signal from the deposited sodium signal.

Our group has already completed laboratory experiments measuring sputter depletion of adsorbed sodium from regolith-like forsterite, and thermal desorption of adsorbed sodium from polished quartz targets. In addition, we intend thermal desorption from polished forsterite targets as well. To complement these future measurements, we attempted to model the thermal desorption of sodium from single-crystal forsterite using molecular dynamics simulations.

Methodology

In order to observe the effects of thermal desorption on Mercury's surface, we ran simulations through the molecular dynamics code called LAMMPS, which stands for the Large-scale Atomic/Molecular Massively Parallel Simulator. LAMMPS has the ability to track the motion of thousands of particles and apply several force fields to the system in order to mimic different situations on the molecular scale. For example, one can model both amorphous and crystalline structures at different temperatures and monitor their changes over time. It can also be run on a single processor or in parallel, which is useful in cutting down run time. For our purposes, we ran LAMMPS simulations on

the University of Virginia's HPC called Rivanna.

In order to accurately model the system, realistic interactions between the particles must be defined through the implementation of force fields called potentials. LAMMPS can apply various potentials to different parts of the system; for our simulations, we needed potentials between each pair of bulk atoms, between each sodium and bulk atom, and between sodium atoms. Defining the correct potential is essentially its own field of study, especially since even the slightest variations in a system will drastically change the interatomic forces at work. Potentials for our specific system have not been found yet, so we chose to combine two known potentials that provided realistic results for similar situations.

For the bulk material, a potential that dealt with solid forsterite was required. The Pedone potential, which was originally developed for oxide glasses, showed to be the second most accurate potential when modeling lattice defects in forsterite (Pedone et al. 2006; Hirel et al. 2021). Equation 1 shows how the potential is calculated as a function of assigned charges (q_i, q_j), separation between the two atoms (r), bond dissociation energy (D_0), equilibrium bond distance (r_0), the function of the potential well slope (α), and the elastic coefficients (B_0).

$$U(r) = \frac{q_i q_j}{r} + D_0[e^{-2\alpha(r-r_0)} - 2e^{-\alpha(r-r_0)}] + \frac{B_0}{r^{12}} \quad (1)$$

Its accuracy was only surpassed by the THB1 potential, but this force field had serious disadvantages like excessive use of computational time and lack of implementation in modern codes (Hirel et al. 2021). Even though our experiments were not explicitly concerned with lattice defects, Pedone was a built in LAMMPS potential that could provide accurate bulk interactions using a reasonable amount of computational time. This potential was also tested for accuracy against well-known laboratory measured bulk parameters such as material density, a pressure range of 0-12 GPa, and stacking faults (Hirel et al. 2021).

The Lennard Jones (LJ) potential with the inclusion of a cutoff distance was selected for the deposited sodium atoms. Known as one of the most common and thoroughly studied potentials, the LJ potential can be properly described in Equation 2, where σ indicates the zero crossing of the y-axis and ε represents the well depth. The first term represents the attractive forces, while the second dictates the repulsive interactions.

$$U(r) = 4\varepsilon[(\frac{\sigma}{r})^{12} - (\frac{\sigma}{r})^{6}] \quad (2)$$

LJ parameters for every combination of particles have unfortunately not been reported as of yet, so with the use of the Lorentz-Berthelot mixing rules, interaction pairs were derived from pre-existing same-particle pair parameters (Lorentz, 1881; Berthelot, 1898). The new ε_{ij} and σ_{ij} parameters for non uniform particle pairs are calculated with Equations 3 and 4.

$$\varepsilon_{ij} = \sqrt{\varepsilon_i \varepsilon_j} \quad (3)$$

$$\sigma_{ij} = \frac{\sigma_i + \sigma_j}{2} \quad (4)$$

Conversely, all *similar* particle pair parameters were found in a universal parameterization file on OpenKIM where ε, σ, and cutoff distance values were defined (https://openkim.org/id/LJ_ElliottAkerson_2015_Universal__MO_959249795837_003).
The only parameter that did not have an explicit mixing rule was the cutoff distance, so we conducted a survey of its effects by running simulations of 10 sodium atoms being deposited on bulk forsterite that was heated at different temperatures. The cutoff distance

that resulted in the Na atoms' most realistic desorption behaviors was chosen, as discussed in the next section.

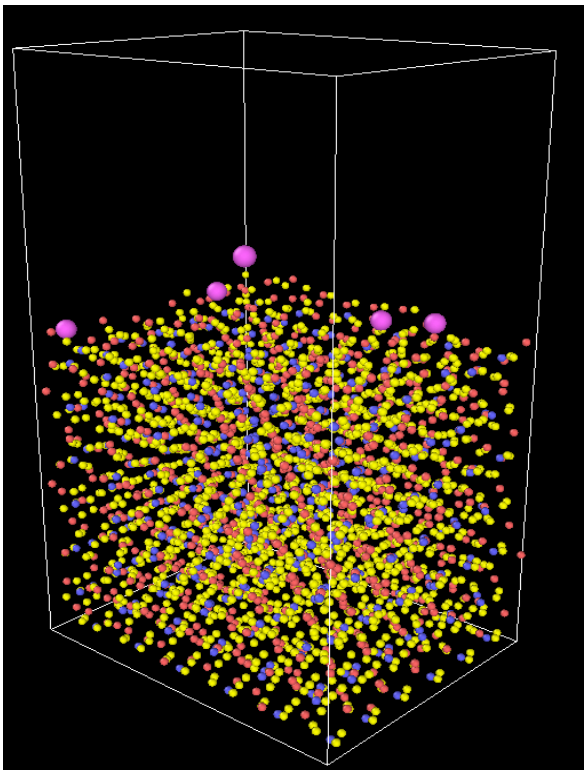

Figure 3 A visualization of a LAMMPS simulation of sodium being deposited on forsterite. The pink atoms are the deposited sodium, the red are the magnesium atoms, the blue are silicon atoms, and the yellow atoms are oxygen.

Now that the optimal potentials were applied, the system must now be prepared for deposition. This requires running three preemptive simulations that aim to equilibrate the system. The first shifts the particles in the simulation box to correspond to the minimum energy state. We then run a fix NVT simulation, which turns the system into a canonical ensemble, and heat up the bulk slowly to the desired temperature. Lastly, a fix NPT is applied to the system to let particles behave as they would in an isothermal-isobaric ensemble. Running these three initial simulations allows the system to run with a correct particle density and behave realistically in the production run. Figures 3 and 4 show a frame of a typical production run from a LAMMPS simulation as seen in OVITO, which is a software that visualizes the data from the simulation dump files.

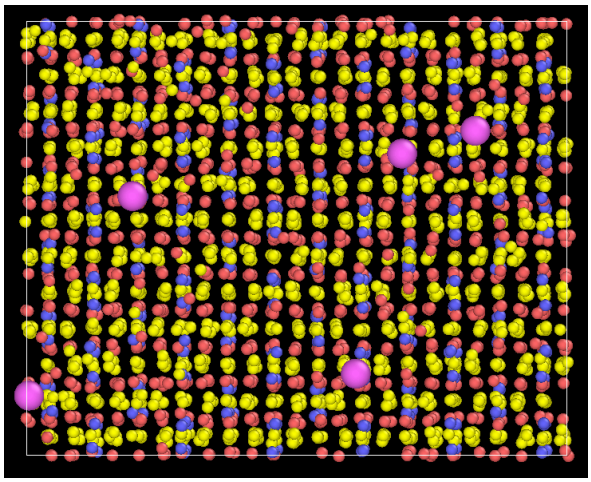

Figure 4 Same as Figure 3 but viewed from above.

Once the production run was completed, properties about each particle in the simulation box were recorded in a dump file. To eliminate any redundancies and allow for efficient data analysis, I wrote a python script that reformatted the information into tabular form and saved the data as a .csv file. The code was fully automated and produced the .csv file in minutes, and it was now possible to easily plot the results.

Results and Discussion

The survey of potential cutoff distances revealed that a uniform cutoff of 2.6 Å across all Na interactions had the most realistic results. The z-positions of all sodium atoms as a function of time at 100, 300, 400, 700, and 1500 K are displayed below in Figures 5-9. All Na atoms were deposited ~11 Å above the surface but were spawned in random positions within the x-y plane.

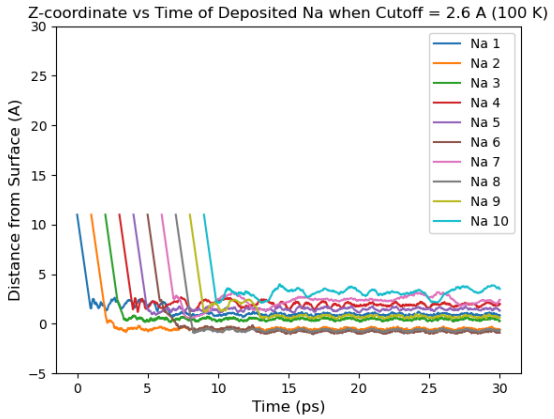

Figure 5 Vertical position of ten deposited Na atoms when surface is heated to 100 K. All atoms remain on the surface after 30 ps.

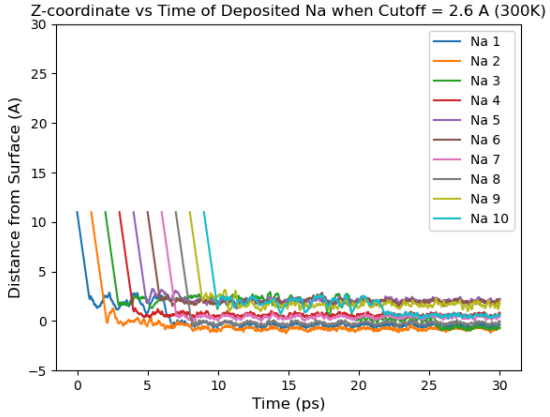

Figure 6 Vertical position of ten deposited Na atoms when surface is heated to 300 K. All atoms remain on the surface after 30 ps.

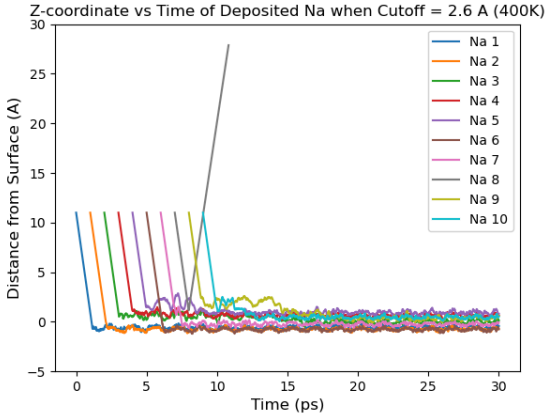

Figure 7 Vertical position of ten deposited Na atoms when surface is heated to 400 K. One Na atom desorbed after 30 ps had passed.

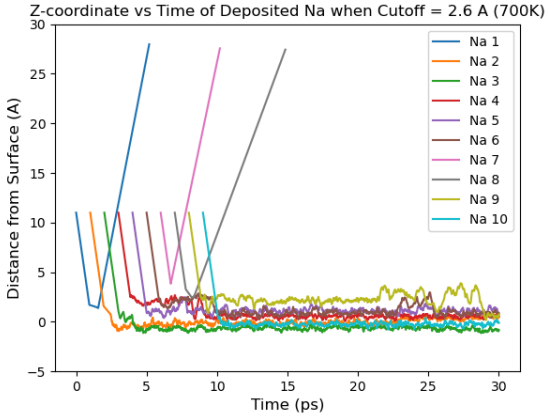

Figure 8 Vertical position of ten deposited Na atoms when surface is heated to 700 K. Three Na atoms desorbed after 30 ps had passed.

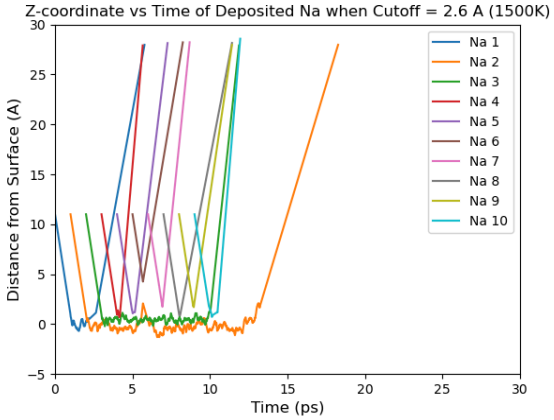

Figure 9 Vertical position of ten deposited Na atoms when surface is heated to 1500 K. All ten Na atoms desorbed after 30 ps had passed.

This cutoff distance (r_c) is relatively small, especially when it is common practice to set it to be 2.5x the value of the σ parameter (Frenkel and Smit, *Understanding Molecular Simulation,* 2002). However, when implementing $r_c > 1.5\sigma$, we observed no desorption, even at 1500 K where it is expected that all Na atoms would desorb quickly. With r_c = 2.6 Å, every Na atom desorbed within the first 15 picoseconds in the 1500 K case, which follows realistic desorption trends. Experimental results also showed that little to no Na desorption should occur at room temperature (about 300 K), which is also the case in Figure 2. Although our measured cutoff has the particles ignore a large portion of the potential curve as a function of atomic separation, it isn't necessarily unphysical. It simply does not meet our initial expectations.

Now that a suitable cutoff distance has been determined, the maximum simulated residence time of the desorbing atoms was calculated. We turned off Na-Na interactions for these simulations since our main priority was to observe how the surface temperature affects the desorption rate of deposited sodium. In a single simulation, 100 atoms were dropped in the first 100 timesteps (we defined a timestep to be 0.001 picoseconds in the parameter file), and their z-coordinates were tracked as they were deposited and potentially ejected from the surface. We ran 10 simulations with a duration of 40 picoseconds for every temperature of interest (300 K, 500 K, and 700 K) which brings our sample size to 1000 deposited sodium atoms per case.

We defined the "surface" as any atoms resting on the forsterite bulk below 38 Å in the simulation box; since none of the deposited Na seem to exceed this z-value when not actively desorbing, it was chosen as the threshold. Residence time was calculated by subtracting the time at which the deposited particle first passed through this threshold value from the time at which it exceeded 38 Å for the final time in the simulation. This method is ideal since behaviors like "hopping" could exist where the atom exceeds the surface threshold briefly, but since only the final time it exceeds 38 Å is considered, residence time is still correctly calculated. See Figures 8-10 for simulation results for all cases.

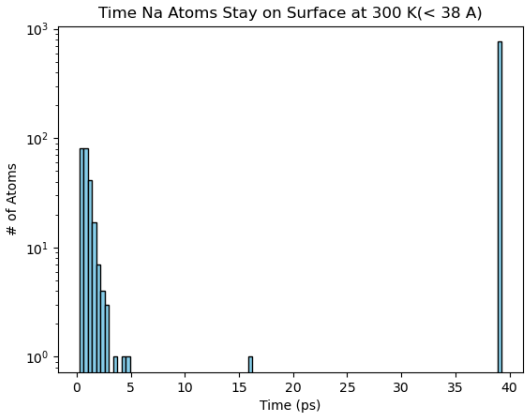

Figure 8 Residence time of sodium on the surface at 300 K. A total of 23.8% of deposited Na desorbed from the surface. The average residence time is 0.982 ps for all desorbing particles.

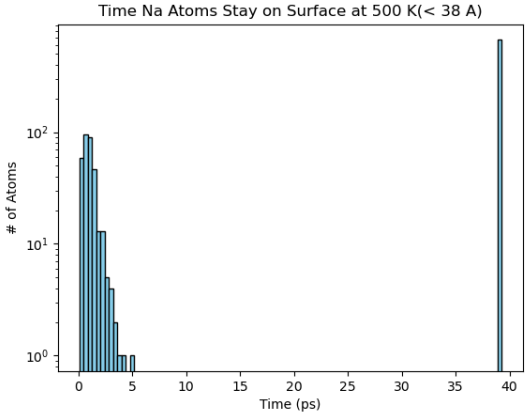

Figure 9 Residence time of sodium on the surface at 500 K. A total of 33.2% of deposited Na desorbed from the surface. The average residence time is 1.030 ps for all desorbing particles.

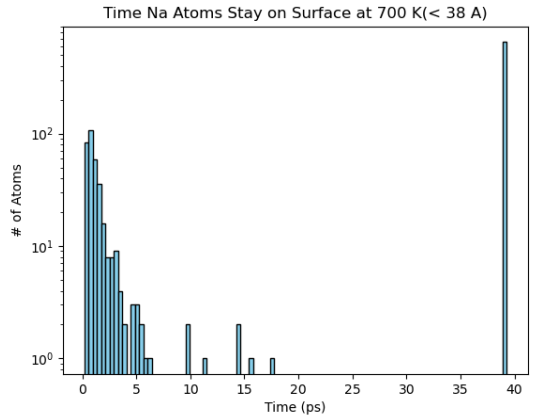

Figure 9 Residence time of sodium on the surface at 700 K. A total of 34.9% of deposited Na desorbed from the surface. The average residence time is 1.419 ps for all desorbing particles.

Once Na is fully situated after ~ 10 ps, it is unlikely that it will desorb later. Either it desorbs in the first 10 ps or permanently resides on the surface with rare exceptions. This is evidence that Na is not very mobile once deposited on the surface, but the bulk temperature plays a major role in determining their desorption rates. We see a trend where the hotter the surface is, a larger percentage of atoms are initially reflected due to the greater momentum of the bulk atoms, as expected. We also observe that the majority of the sodium atoms remain on the surface at least beyond the duration of our simulations, regardless of bulk temperature. However, we would expect for atoms to desorb more quickly when the temperature is increased; instead we see a greater lag in average desorption time. This may be due to the insufficient statistics. More simulations will be run at these temperatures to increase the sample size and gather more accurate data. Sporadic counts after ~10 ps may be representative of the beginnings of desorption distributions, but better resolution is required to be confident in these claims.

To improve future results, we learned that deposited Na sample size must be increased to achieve better statistics. Further research must be done to find the most accurate potentials as well. Although a patchwork of potentials may adequately represent physical reality, the reduced cutoff distances they require in our case leads us to believe that there may be more appropriate candidates. We also intend to extend our cutoff value search by lifting the requirement that the cutoff distances need to be the same for every sodium interaction. We implemented this rule for simplicity's sake, but there is no physical reason for the LJ interactions to all have the same cutoff. Finally, as mentioned before, additional laboratory experiments will be conducted in order to compare with the simulation results. This will lead to a better understanding of current and future exospheric data, and guide research into similar processes on other airless bodies.

References

Berthelot, D.: Sur le Mélange des Gaz. Comptes Rendus de l'Académie des Sciences Paris, 126, 1703 (1889).

Cassidy, T. A., McClintock, W. E., Killen, R. M., Sarantos, M., Merkel, A. W., Vervack, R. J., & Burger, M. H. (2016). A cold-pole enhancement in Mercury's sodium exosphere. *Geophysical Research Letters*, *43*(21), 11,121-11,128. https://doi.org/10.1002/2016GL071071

Domingue, D. L., & Russell, C. T. (2007). *The MESSENGER mission to Mercury* (D. L. Domingue & C. T. Russell, Eds.). *Springer Science & Business Media.* https://doi.org/10.1007/978-0-387-77214-1

Frenkel, D., & Smit, B. (2002). Understanding Molecular Simulation. *Elsevier*. https://doi.org/10.1016/b978-0-12-267351-1.x5000-7

Hirel, P., Furstoss, J., & Philippe Carrez. (2021). A critical assessment of interatomic potentials for modelling lattice defects in forsterite Mg$$_2$$SiO$$_4$$ from 0 to 12 GPa. Physics and Chemistry of Minerals, 48(12). https://doi.org/10.1007/s00269-021-01170-6.

Hundhausen, A. J., Bame, S. J., Asbridge, J. R., & Sydoriak, S. J. (1970). Solar wind proton properties: Vela 3 observations from July 1965 to June 1967. *Journal of Geophysical Research*, 75(25), 4643–4657. https://doi.org/10.1029/JA075I025P04643

King, J. H., & Papitashvili, N. E. (2005). Solar wind spatial scales in and comparisons of hourly Wind and ACE plasma and magnetic field data. *Journal of Geophysical Research: Space Physics*, 110(A2), 2104. https://doi.org/10.1029/2004JA010649

Lorentz, H. A. (1881). "Ueber die Anwendung des Satzes vom Virial in der kinetischen Theorie der Gase". *Annalen der Physik*. **248** (1): 127–136. Bibcode:1881AnP...248..127L. https://doi.org/10.1002%2Fandp.18812480110.

Pedone, A., Gianluca Malavasi, Maria Cristina Menziani, and, & Segre, U. (2006). A New Self-Consistent Empirical Interatomic Potential Model for Oxides, Silicates, and Silica-Based Glasses. *Journal of Physical Chemistry B*, 110(24), 11780–11795. https://doi.org/10.1021/jp0611018

Szalay, J. R., et al. (2018) Dust Phenomena Relating to Airless Bodies. *Space Science Reviews*, vol. 214, no. 5, https://doi.org/10.1007/s11214-018-0527-0.

Szabo, P., Chiba, R., Biber, H., Stadlmayr, R,. Berger, B., Mayer, D,. Mutzke, A., Doppler, M., Sauer, M,. Appenroth, J., Fleig, J., Foelske-Schmitz, A., Hutter, H., Mezger, K., Lammer, H., Galli, A., Wurz, P., Aumayr, F. Solar wind sputtering of wollastonite as a lunar analogue material – Comparisons between experiments and simulations, Icarus, Volume 314, 2018, Pages 98-105, ISSN 0019-1035, https://doi.org/10.1016/j.icarus.2018.05.028.

S. Verkercke, Leblanc, F., J.‐Y. Chaufray, Morrissey, L., Sarantos, M., & Prem, P. (2024). Sodium Enrichment of Mercury's Subsurface Through Diffusion. *Geophysical Research Letters*, 51(21). https://doi.org/10.1029/2024gl109393.

Wurz, P., Fatemi, S., Galli, A., Halekas, J., Harada, Y., Jäggi, N., Jasinski, J., Lammer, H., Lindsay, S., Nishino, M. N., Orlando, T. M., Raines, J. M., Scherf, M., Slavin, J., Vorburger, A., & Winslow, R. (2022). Particles and Photons as Drivers for Particle Release from the Surfaces of the Moon and Mercury. *Space Science Reviews* 2022 218:3, 218(3), 1–83. https://doi.org/10.1007/S11214-022-00875-6.